Localization renormalization and quantum Hall systems

Bartholomew Andrews,[1,2,*] Dominic Reiss,[1,*] Fenner Harper,[1] and Rahul Roy[1,†]
[1]*Department of Physics and Astronomy, University of California at Los Angeles, 475 Portola Plaza, Los Angeles, California 90095, USA*
[2]*Department of Physics, University of California at Berkeley, 100 South Dr, Berkeley, California 94720, USA*

(Received 21 October 2023; revised 24 February 2024; accepted 28 February 2024; published 19 March 2024)

The obstruction to constructing localized degrees of freedom is a signature of several interesting condensed matter phases. We introduce a localization renormalization procedure that harnesses this property and apply our method to distinguish between topological and trivial phases in quantum Hall and Chern insulators. By iteratively removing a fraction of maximally localized orthogonal basis states, we find that the localization length in the residual Hilbert space exhibits a power-law divergence as the fraction of remaining states approaches zero, with an exponent of $\nu = 0.5$. In sharp contrast, the localization length converges to a system-size-independent constant in the trivial phase. We verify this scaling using a variety of algorithms to truncate the Hilbert space and show that it corresponds to a statistically self-similar expansion of the real-space projector. This result is in accord with a renormalization group picture and motivates the use of localization renormalization as a versatile numerical diagnostic for quantum Hall systems.

DOI: 10.1103/PhysRevB.109.125132

I. INTRODUCTION

Renormalization group (RG) approaches are widely employed to distill the essential information from complex configurations and are an invaluable tool for studying the universal properties of systems close to criticality [1–5]. Generally, when scaling relations indicate that a correlation length is the only relevant length scale close to a phase transition, we can leverage the statistical self-similarity of fluctuations up to this correlation scale, by gradually eliminating correlated degrees of freedom at all microscopic lengths. This is the basis of Kadanoff-Wilson RG, which is ubiquitous across a diverse body of research [6]. In recent years, a specific class of phase transitions, distinguished by the divergence or saturation of a characteristic localization length, which we call "localization transitions," has attracted renewed interest. Examples include transitions arising from the topology-localization dichotomy, such as the plateau transition [7–10], and those related to exotic localization phenomena, such as the thermal-MBL crossover [11–14]. In these systems, it is natural to construct a renormalization procedure based explicitly on the localization length to describe the critical phenomena. In analogy to traditional RG, when scaling relations indicate that the localization length is the pertinent length scale close to a phase transition, we can renormalize the system by gradually eliminating *localized* degrees of freedom, which has analogous implications on the statistical self-similarity of the localized removal basis. In light of current research [11,15–19], there is motivation to leverage the localization properties of critical systems in numerical methods and apply such a procedure to study the growing array of localization transitions.

In this paper, we introduce a localization renormalization formalism and apply it to a selection of single-particle examples. Specifically, we focus on phase transitions resulting from the topology-localization dichotomy in quantum Hall systems. By iteratively removing the maximally localized states from distinct sites in the system, we can induce a localization transition with a scaling given by the power-law divergence $\lim_{\rho\to 0, L\to\infty} \xi(\rho) \sim \rho^{-0.5}$, where ξ is the localization length in the residual Hilbert space, ρ is the fraction of states remaining, and L is the linear system size. In contrast, the localization length converges to a system-size-independent constant in the trivial phase. We show that this scaling holds irrespective of the model used to describe the system, the metric used to quantify the localization length, and the way in which states are removed. Furthermore, we examine the expansion of the projector corresponding to the elimination of an orthogonal subset of maximally localized states. Here, we reveal a direct correspondence between the power-law divergence of the localization length and a statistically self-similar expansion of the projector in real space. These results are in accord with an RG picture, where the effective length scale per state is increased by a factor of $\rho^{-1/2}$ on each step and topological phases are identified by the presence of a phase transition. Apart from shedding additional light on the properties of integer quantum Hall systems, localization renormalization may be utilized as a numerical tool to characterize a wide variety of localization-delocalization transitions, including those in topologically trivial systems.

The structure of this paper is as follows. In Sec. II, we define the localization renormalization procedure and in Sec. III we apply it to single-particle case studies, representing continuous and discrete quantum Hall systems. In Sec. IV, we then discuss the interpretations and scope of our results and finally, in Sec. V, we summarize the conclusions and outlook.

*These authors contributed equally to this work.
†rroy@physics.ucla.edu

II. LOCALIZATION RENORMALIZATION

We consider a d-dimensional quantum system, with single-particle Hilbert space $\mathcal{H}$, occupying a real-space region $A \in \mathbb{R}^d$ of linear extent L. To simply illustrate the steps, we focus on single-component single-particle orbitals residing in an isolated band.

We start by identifying a complete basis of wave functions for a given band $\{|\psi\rangle\}$. These single-particle orbitals are confined to regions surrounding points in space or sites on a lattice and are maximally localized according to a real-space metric—conventionally, the distance-squared metric [20]. We emphasize that this basis does not need to be exponentially localized, as this is not always possible, such as for quantum Hall systems [21].

We then define a family of projectors $P_\rho : \rho \in [0, 1]$, which remove a fraction $1 - \rho$ of the maximally localized single-particle basis, such that

$$P_\rho = P_{\text{band}} - \sum_{i \in \mathcal{L}_\rho} |\tilde{\psi}_i\rangle\langle\tilde{\psi}_i|, \tag{1}$$

where P_{band} is a projector onto the relevant single-particle band and $|\tilde{\psi}_i\rangle$ is the symmetrically orthogonalized wave function at site i in the removal subregion $\mathcal{L}_\rho$, which satisfies $|\mathcal{L}_\rho| \leqslant |\mathcal{L}_0| \leqslant |A|$ [22]. We note that, although the states in the basis are generally linearly independent, they are not mutually orthogonal, and so we first need to symmetrically orthogonalize the removal states, such that $\{|\psi\rangle\} \to \{|\tilde{\psi}\rangle\}$. Details of the symmetric orthogonalization procedure are given in Sec. SI of the Supplemental Material [23]. Crucially, since the quasilocal projector $|\tilde{\psi}_i\rangle\langle\tilde{\psi}_i|$ corresponds to the number operator n_i for the single-particle orbital at site $i \in \mathcal{L}_\rho$, the overall projector P_ρ restricts the system to a Hilbert space in which these operators have a fixed (zero) eigenvalue. Hence, by eliminating a maximally localized orthogonal subset of states in the basis, we truncate the Hilbert space $\mathcal{H} \to \mathcal{H}'$.

Provided the family of projectors P_ρ are statistically self-similar under this decimation, we can relate the truncated system $\bar{H}(r) = P_\rho H(\mathbf{r}) P_\rho$ to the original system $H(\mathbf{r})$ by a rescaling $\mathbf{r}' = b\mathbf{r}$ and renormalization $H'(\mathbf{r}') = \zeta^{-1}\bar{H}(\mathbf{r}')$. In this way, we can consider the ground state of $H'(\mathbf{r}')$ as the new ground state defined on the space of states [24]. We then iterate this process to construct a renormalization flow, based on the removal of maximally localized single-particle orbitals, which we call "localization renormalization."

For the case of quantum Hall systems, we deduce the rescaling and renormalization factors to be $b = \rho^{-1/2}$ and $\zeta = \rho$, respectively. In particular, we observe a divergence of the localization length in the $\rho \to 0, L \to \infty$ limits, governed by a universal scaling exponent $\nu \sim 1/2$ for topological bands, whereas we observe convergence to a system-size-independent constant in the trivial phase. This holds independently of how the single-particle states are removed and how the localization length is defined.

III. QUANTUM HALL EXAMPLES

In this section, we demonstrate the localization renormalization procedure through the use of two examples, based on the integer quantum Hall effect. In Sec III A, we examine continuous systems in the form of Landau levels and, in Sec. III B, we examine discrete systems in the form of Chern insulators.

A. Landau levels

To begin, we focus on Landau levels. In Sec. III A 1, we summarize the Landau level Hamiltonian and properties of coherent states, in Sec. III A 2, we explain the state removal algorithm and, in Sec. III A 3, we present numerical results for the localization renormalization.

1. Model

We consider a free spinless electron of mass m_e and charge $-e$, confined to the xy plane, in the presence of a perpendicular magnetic field $\mathbf{B} = B\hat{\mathbf{e}}_z$. The Hamiltonian is given as $H_{\text{LL}} = \boldsymbol{\pi}^2/2m_e$, where $\boldsymbol{\pi} = \mathbf{p} - e\mathbf{A}$ is the dynamical momentum, $\mathbf{p}$ is the canonical momentum, and $\mathbf{A}$ is the vector potential. Since π_x and π_y are canonical conjugates, this Hamiltonian has the same structure as a harmonic oscillator, such that $H_{\text{LL}} = \hbar\omega_c(a^\dagger a + 1/2)$, where ω_c is the cyclotron frequency and $a^{(\dagger)}$ are the ladder operators hopping between energy levels. The eigenspectrum is composed of evenly spaced and highly degenerate Landau levels at energies $E_n = \hbar\omega_c(n + 1/2)$, where n is the Landau level index. Using symmetric gauge, we may simply express the angular momentum operator as $L_z = \hbar(a^\dagger a - b^\dagger b)$, where we have introduced the ladder operators $b^{(\dagger)}$, defined using center coordinates $\mathbf{R}$ conjugate to $\boldsymbol{\pi}$, governing the angular momentum quantum number m. Hence the Landau level states are conventionally indexed as $|n, m\rangle$ [25,26].

The coordinate representation of a Landau level wave function may be obtained by solving the differential equation $a|0, m\rangle = b|n, 0\rangle = 0$ in an appropriate basis and can be subsequently translated through a distance $\boldsymbol{\delta}$ using the magnetic translation operator $t(\boldsymbol{\delta}) = \exp(-\mathrm{i}\boldsymbol{\delta} \cdot \mathbf{K}/\hbar)$, where $\mathbf{K} = \mathbf{p} - e\mathbf{A} + e\mathbf{B} \times \mathbf{r}$ is the pseudomomentum, which commutes with the Hamiltonian. In symmetric gauge, the Landau level states take the form of a Gaussian, modulated by Laguerre polynomial and monomial prefactors [25]. From the eigenspectrum of the angular momentum operator, we can see that the most-localized Landau level states are obtained at $n = m$ with second moment $\langle n, n|r^2|n, n\rangle = 2(2n + 1)\ell^2$, where ℓ is the magnetic length. For example, the most-localized state in the lowest Landau level (LLL) is given in a coordinate representation as $\phi_{0,0}(\mathbf{r}) \sim \exp(-r^2/4\ell^2)$ with a second moment $\langle 0, 0|r^2|0, 0\rangle = 2\ell^2$.

In this section, we focus our attention on coherent states, which are nondispersive wave packets that saturate the uncertainty principle and correspond to classical observable evolution. Formally, these states are defined as eigenstates of the lowering operator. Since we restrict ourselves to a single Landau level, we consider the eigenstates of $b|\beta\rangle = \beta|\beta\rangle$, where $|\beta\rangle$ is a coherent state with corresponding eigenvalue β. Coherent states have several important properties for this study. In particular, since the ladder operators $b^{(\dagger)} = \frac{1}{\sqrt{2}}(X + \mathrm{i}Y)^{(\dagger)}$ are defined using the center coordinates $\mathbf{R}$, saturating the Heisenberg uncertainty principle corresponds to $\Delta X \Delta Y = \hbar/2$. Hence a coherent state in a Landau level is necessarily a maximally localized state and so may be

obtained by magnetically translating the $n = m$ Landau level states, described above [27]. Removing maximally localized states in Landau levels is the main step of our Hilbert space truncation algorithm, outlined in Sec. III A 2.

Finally, we note that coherent states trivially form an overcomplete basis for a given Landau level, since they are enumerated by an uncountable set, whereas the orthogonal basis of angular momentum eigenstates is countable. Therefore, it is desirable to truncate the set of coherent states to obtain a complete basis. Indeed, it has been shown that we can form a critical basis set by restricting coherent states to the sites of a grid in the XY plane of unit cell area $S = 2\pi$ and an overcomplete set with $S < 2\pi$ [28–30]. By removing just one state from the critical set, we can make the set exactly complete. However, naïvely attempting to symmetrically orthogonalize such a complete set of coherent states in a Landau level compromises locality. It has been shown that the resulting states have a high overlap with Gaussian states at short distances from the origin, but an oscillating power-law decay at long distances with a diverging second moment [21]. This highlights the topology-localization dichotomy: it is impossible to construct exponentially localized Wannier functions in a topological system.

2. Method

Having shown that a critical set of maximally localized Landau level states may be obtained using a grid of coherent states in the XY plane with a unit cell area of 2π, we can utilize this in our Hilbert space truncation algorithm. In this procedure, we simultaneously remove the most-localized states on the sites of a square grid, converging from an arbitrarily large unit cell area to the unit cell area corresponding to this critical set. However, we note that the results hold independently of the truncation algorithm and removal grid geometry, as demonstrated in Secs. SII and SIII of the Supplemental Material [23]. The method is as follows.

We work in a Landau level $|n, m\rangle$ defined on a continuous disk of radius R, centered at the origin. In each Landau level n, we use a truncated angular momentum basis $m \in \{0, 1, \ldots, \frac{3}{4}R^2\}$. The basis cutoff is chosen based on empirical convergence, such that the critical grid of wave packets on the disk is approximately homogeneous and not distorted by the boundary. Next, we introduce a removal lattice $\mathcal{L}_\rho$ with sites on a square grid

$$\mathbf{r}_{ij} = a_\rho[(i - 1/2)\hat{\mathbf{e}}_x + (j - 1/2)\hat{\mathbf{e}}_y], \tag{2}$$

where $a_\rho = \sqrt{2\pi/(1-\rho)}$ is the lattice constant and $i, j \in \mathbb{Z}$, as sketched in Fig. 1. The quantity ρ is the fraction of states remaining relative to $\mathcal{L}_0$, defined as $\rho = 1 - A_0/A_\rho \in [0, 1]$. For each lattice site $\mathbf{r}_{ij} \in \mathcal{L}_\rho$, we then find the maximally localized state $|\psi_{ij}\rangle$, which in this case is given by the Landau level coherent state.

This defines the set of maximally localized states in a Landau level for each ρ. However, although these states are generally linearly independent, they are not mutually orthogonal. Therefore, in order to project these states out of the Hilbert space, we first need to orthogonalize the subspace. To this end, we use the symmetric orthogonalization procedure to transform $\{|\psi\rangle\} \to \{|\tilde{\psi}\rangle\}$. We can then apply the projector

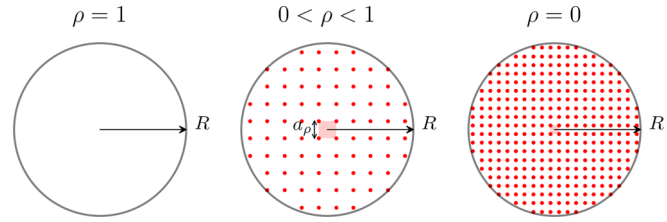

FIG. 1. Removal lattice for Landau levels. Convergence of the removal lattice $\mathcal{L}_\rho$ in Landau levels, sketched for three values of ρ. The area of the $\mathcal{L}_\rho$ unit cell $a_\rho^2 = 2\pi/(1-\rho)$ is shaded pink and the disk radius R is marked with an arrow.

$$P_\rho^{\mathrm{LL}} = P_{n\mathrm{LL}} - \sum_{i,j\in\mathcal{L}_\rho} |\tilde{\psi}_{ij}\rangle\langle\tilde{\psi}_{ij}|, \tag{3}$$

where $P_{n\mathrm{LL}}$ is the projector to the nth Landau level.

Finally, on each removal iteration we record the localization length of the system ξ. Note that we have offset the removal lattice from the origin, as shown in Eq. (2), so that we can use this as our reference site for the most-localized state in the system. The origin is also furthest away from the boundary of the disk and hence least susceptible to finite-size effects. Although there are many metrics for quantifying the localization length, we choose the minimum eigenvalue of the distance-squared matrix [20], such that $D^2 = P_\rho^{\mathrm{LL}}\mathbf{r}^2 P_\rho^{\mathrm{LL}}$. A discussion of metrics for the localization length is presented in Sec. SIV of the Supplemental Material [23].

In summary, we identify the maximally localized states $\{|\psi\rangle\}$ at sites $\mathbf{r}_{ij} \in \mathcal{L}_\rho$, after which we symmetrically orthogonalize the states $\{|\psi\rangle\} \to \{|\tilde{\psi}\rangle\}$, project them out of the system using P_ρ^{LL}, and subsequently compute the localization length ξ, corresponding to the second moment of the maximally localized state at the origin. We start at $\rho \lesssim 1$ and then repeat for decreasing ρ, taking the limit $\rho \to 0$, which corresponds to eliminating a critical basis of states and hence a localization length divergence.

3. Results

After iteratively performing this state removal, we can plot the behavior of ξ as a function of ρ in each case. In the left panels of Fig. 2, we show the scaling of $\xi(\rho)$ at various system sizes R, in the (a) $n = 0$, (b) $n = 1$, and (c) $n = 2$ Landau levels. From the figures, we can see a divergence of the localization length in the $\rho \to 0$ and $R \to \infty$ limits [31]. In order to quantify this divergence, we perform a finite-size scaling analysis. By finding a dimensionless scaling function g, which satisfies

$$\xi(\rho)/\xi_\infty(\rho) = g(R/\xi_\infty(\rho)), \tag{4}$$

where ξ_∞ is the extrapolated localization length in the thermodynamic limit, we can verify the power-law divergence $\lim_{\rho\to 0}\xi(\rho) \sim \rho^{-\nu}$. Furthermore, by quantifying how well the data from Eq. (4) collapse onto the same curve, we can compute the scaling exponent ν [32]. Minimizing a quality metric of data collapse $d(\nu)$ [33] yields the scaling exponent in each case, as shown in the right panels of Fig. 2. The computed values, $\nu_{0\mathrm{LL}} = 0.500 \pm 0.005$, $\nu_{1\mathrm{LL}} = 0.500 \pm 0.006$,

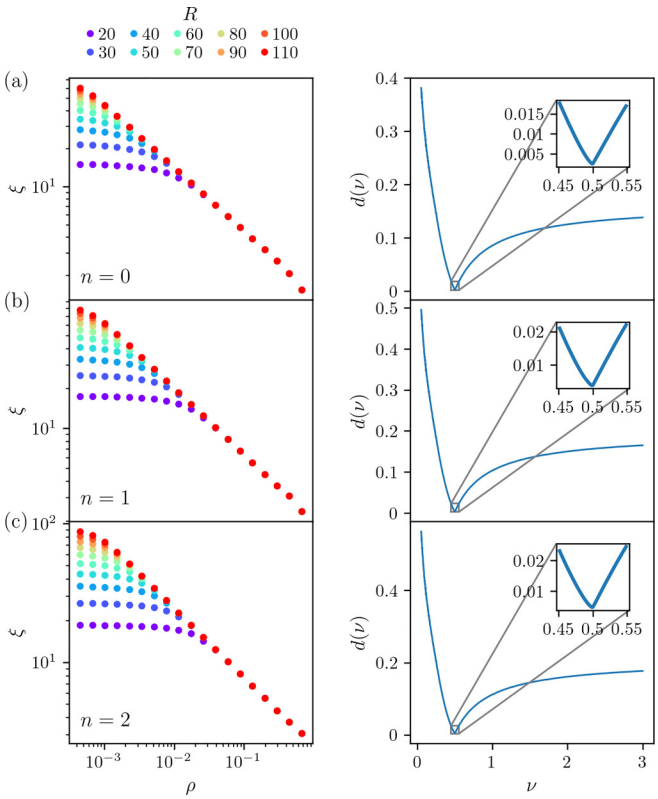

FIG. 2. Localization scaling in Landau levels. (Left) Localization length $\xi(\rho)$ obtained by the simultaneous elimination of a lattice of localized states in the (a) $n = 0$, (b) $n = 1$, and (c) $n = 2$ Landau levels. The system size R is depicted in different colors. At small ρ and large system sizes, the relationship is linear indicating power-law behavior in the thermodynamic limit. (Right) The quality function of data collapse $d(\nu)$ for the (a) $n = 0$, (b) $n = 1$, and (c) $n = 2$ Landau levels; optimization of the quality function results in critical exponents of (a) $\nu_{0\mathrm{LL}} = 0.500 \pm 0.005$, (b) $\nu_{1\mathrm{LL}} = 0.500 \pm 0.006$, and (c) $\nu_{2\mathrm{LL}} = 0.500 \pm 0.006$.

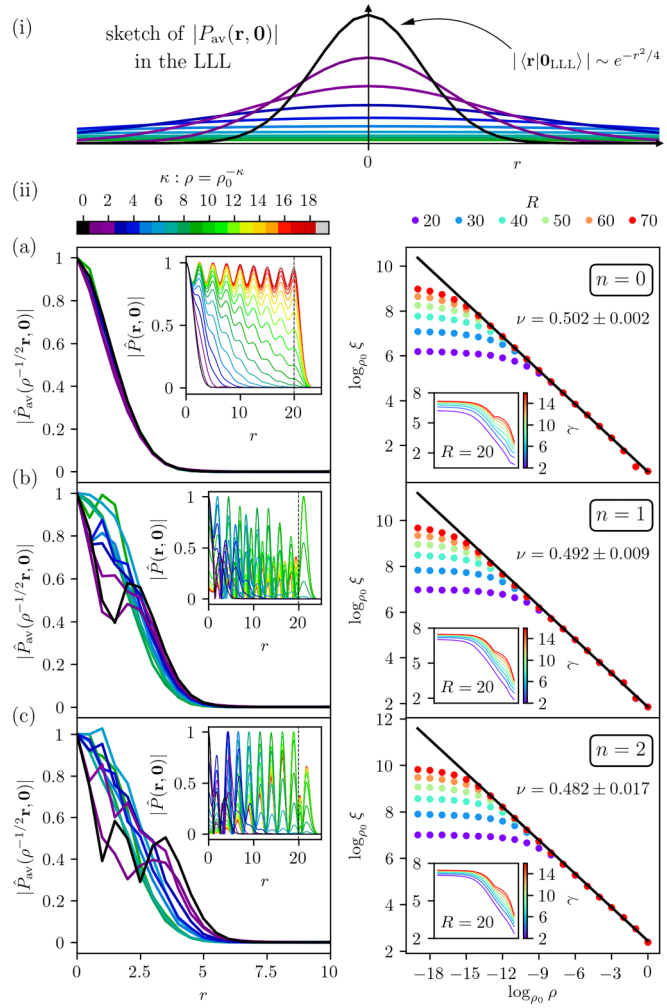

FIG. 3. Projector expansion in Landau levels. (i) Sketch of the averaged real-space projector expansion as $\rho \to 0$ in the LLL. (ii) (Left) Real-space radial profile of the projector $P(\mathbf{r}, \mathbf{0}) = \langle\mathbf{r}|P_\rho^{\mathrm{LL}}|\mathbf{0}\rangle$. The rotationally and translationally averaged projector, normalized with respect to the initial value, $\hat{P}_{\mathrm{av}}$, is shown in the main plot. The original unaveraged projector, normalized with respect to the maximum value, $\hat{P}$, is shown inset. The projectors are presented for the (a) $n = 0$, (b) $n = 1$, and (c) $n = 2$ Landau levels, at a system size of $R = 40$ in the main plot and $R = 20$ in the inset, with $\rho_0 = 1.5$. The boundary of the system at $r = 20$ in the inset is marked with a dashed line. Note that the projectors are plotted in reverse order, such that the $\kappa = 0$ line is on top. (ii) (Right) Finite-size scaling of the second moment of the projector for the (a) $n = 0$, (b) $n = 1$, and (c) $n = 2$ Landau levels. The lines of best fit, for the linear region of the largest system size, are overlaid in black. The corresponding higher moments, $\xi^\gamma = \langle r^\gamma \rangle$, are shown inset for $R = 20$.

and $\nu_{2\mathrm{LL}} = 0.500 \pm 0.006$, are in accord precisely with a scaling exponent of $\nu = 0.5$ in each case, with only minor discrepancies due to numerical imprecision. Here, the error bars are given as the 1% fluctuations of the quality metric about the minimum, computed using the Hessian $d''(\nu)$. Further details on the finite-size scaling analysis are given in Sec. SV of the Supplemental Material [23].

To gain further insight on the nature of this scaling, we examine the projector P_ρ^{LL} at each step, as sketched in Fig. 3(i). In the left panels of Fig. 3(ii), we show the magnitude of the projector in real space, relative to the origin, $|P(\mathbf{r}, \mathbf{0})| = |\langle\mathbf{r}|P_\rho^{\mathrm{LL}}|\mathbf{0}\rangle|$ in the (a) $n = 0$, (b) $n = 1$, and (c) $n = 2$ Landau levels. Starting with the inset of Fig. 3(ii)(a), we present the normalized projector $|\hat{P}| \sim \rho^{-1}|P|$ for various ρ in the smallest system size $R = 20$. At $\rho = 1$, we start with the Gaussian state at the origin and on each removal iteration the projector expands, continuing until the edge of the system ($r = 20$) is reached at $\rho \approx 1.5^{-9}$. This corresponds to the value of ρ where the linear scaling breaks down in Fig. 2(a). We note also that there are slight oscillations in the amplitude of $\hat{P}$ with length scale $a_0 = \sqrt{2\pi}$, corresponding to the modulation of the removal lattice $\mathcal{L}_0$. Crucially, in the right panel of Fig. 3(ii)(a), we plot the localization length quantified via the second moment of the projector against ρ and show that we can recover the same scaling exponent. In the inset of the right panel of Fig. 3(ii)(a), we further show that this scaling relation is not only recovered from the second moment but also for higher moments, $\gamma \lesssim 10$ [34]. This indicates that the projector is self-similar in a statistical sense [35]. Further details of the moment computations are provided in Sec. SVI of the Supplemental Material [23]. Finally, to elucidate this

statistical self-similarity, we can rescale the family of projectors P_ρ^{LL} to show that they collapse onto the same curve. In the left panel of Fig. 3(ii)(a), we present the translationally and rotationally averaged normalized projector $\hat{P}_{\mathrm{av}}$, which eliminates any artifacts specific to the removal lattice, and we plot this using the rescaled spatial coordinates $\mathbf{r}' = \rho^{-1/2}\mathbf{r}$. Here, we clearly observe that the projectors collapse onto the initial Gaussian. In higher Landau levels, this picture also holds, albeit slightly obscured by the complexity of our initial coherent state $|\langle \mathbf{r}|\mathbf{0}_{n\mathrm{LL}}\rangle| \sim e^{-r^2/4}|L_n(r^2/2)|$, where L_n is the nth Laguerre polynomial. Again, we find that the second moment of the expanding projector can be used as a proxy for the localization to extract the scaling exponent, as shown in the right panels of Figs. 3(ii)(b) and 3(ii)(c). Moreover, the projector is statistically self-similar up to high moments $\gamma \lesssim 10$, as shown in the insets. Rescaling the projector, as before, we find that the curves approximately collapse onto a single Gaussian, as shown in the left panels of Figs. 3(ii)(b) and 3(ii)(c); however, this is now more difficult to discern visually due to the Laguerre polynomial modulation in the initial coherent state. In all cases, we obtain a scaling exponent $\nu \simeq 0.5$ from the self-similar projector expansion. Although this is numerically more challenging to extract for higher Landau levels, all three computed values agree within error bars.

B. Chern insulators

To complement this analysis, we now focus on Chern insulators. In Sec. III B 1, we define the tight-binding model, in Sec. III B 2, we outline the truncation algorithm for discrete systems and, in Sec. III B 3, we present results for the scaling exponent.

1. Model

We consider a free spinless electron confined to a lattice on the xy plane. One of the most well-understood examples of a Chern insulator is the Haldane model [36], defined on the honeycomb lattice as

$$H_{\mathrm{CI}} = -t_1 \sum_{\langle ij\rangle} c_i^\dagger c_j - t_2 \sum_{\langle\langle ij\rangle\rangle} e^{\pm i\phi} c_i^\dagger c_j + M \sum_i (n_{A,i} - n_{B,i}) + \mathrm{H.c.}, \tag{5}$$

where t_1 and t_2 are the amplitudes corresponding to nearest- ($\langle ij\rangle$) and next-nearest-neighbor ($\langle\langle ij\rangle\rangle$) hoppings, $c^{(\dagger)}$ are the spinless fermion creation (annihilation) operators, $e^{\pm i\phi}$ is the next-nearest-neighbor complex phase factor, M is the staggered chemical potential, and $n_{A(B)}$ is the density operator on sublattice A (B). The sign of the complex phase is determined by the direction of the next-nearest-neighbor hopping. The phase is positive clockwise around a minimal down-pointing triangle of the A sublattice and counterclockwise around a minimal down-pointing triangle of the B sublattice. By carefully selecting the parameters in the Haldane model, we can tune between a topological and trivial phase.

For consistency with our state removal algorithm defined for Landau levels in Sec. III A 2, we map the Haldane model onto a square lattice with orthogonal basis vectors $\mathbf{a}_1 \cdot \mathbf{a}_2 = 0$, as depicted in Fig. 4(a). Although the geometry of the model changes under this mapping, with nearest- and next-nearest neighbors no longer preserved, the topology is unchanged [37]. Specifically, we obtain the same Haldane lobe phase diagram in the M/t_2 against ϕ parameter plane. The Haldane Hamiltonian yields a two-band eigenspectrum, where the bottom band has Chern number $C_1 = -1$ for $|M/t_2| \leqslant 3\sqrt{3}\sin(\phi)$ with $\phi \in (-\pi, 0)$, $C_1 = 1$ for $|M/t_2| \leqslant 3\sqrt{3}\sin(\phi)$ with $\phi \in (0, \pi)$, and $C_1 = 0$ elsewhere. In this section, we restrict ourselves to the physics of the lowest band and study three configurations, $\mathbf{t}_a$ (topological), $\mathbf{t}_b$ (topological), and $\mathbf{t}_c$ (trivial), as shown in Fig. 4(b). Further details on the choice of parameters are discussed in Sec. SVII of the Supplemental Material [23]. We note that the localization renormalization described in this section works for any choice of Chern insulator. We choose the Haldane model due to its popularity, motivated particularly by recent realizations in moiré materials [38] and theoretical studies of its topological phase transitions [19].

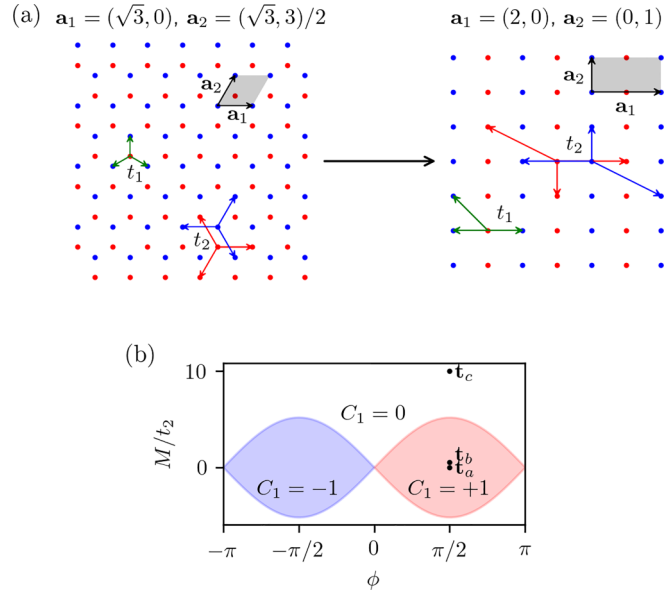

FIG. 4. Haldane model on a square lattice. (a) Mapping of the Haldane model onto a square lattice. The basis vectors $\{\mathbf{a}_1, \mathbf{a}_2\}$ are given in units of the lattice constant and the unit cell is shaded gray. The t_1 hoppings are colored green and the t_2 hoppings are colored red (blue) according to their A (B) sublattice, with the direction of the arrows corresponding to a positive complex phase. (b) Phase diagram for the Haldane model, as a function of complex phase ϕ and chemical potential M, colored according to the sign of the Chern number for the lowest band C_1. The three selected parameter sets are at $\mathbf{t}_a = \{t_2 = 0.1, M = 0\}$, $\mathbf{t}_b = \{t_2 = 0.2, M = 0.1\}$, and $\mathbf{t}_c = \{t_2 = 0.1, M = 1\}$. For all parameter sets, $\phi = \pi/2$, and in all cases we set $t_1 = 1$.

2. Method

The method is similar to the procedure described for Landau levels in Sec. III A 2. However, there are a few technical nuances specific to discrete systems that increase the complexity in this case. As before, the renormalization is independent of the details of the algorithm, as shown in Secs. SII

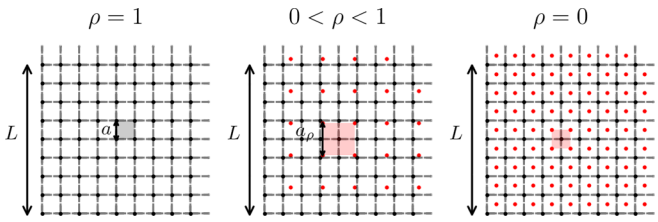

FIG. 5. Removal lattice for the Haldane model. Convergence of the removal lattice $\mathcal{L}_\rho$ for the square-lattice Haldane model, sketched for three values of ρ. The area of the $\mathcal{L}$ unit cell $a^2 = 1$ is shaded gray, the area of the $\mathcal{L}_\rho$ unit cell $a_\rho^2 = 1/(1-\rho)$ is shaded pink, and the linear system size L is marked with an arrow.

and SIII of the Supplemental Material [23]. The method is as follows.

We start with an underlying square lattice for the Haldane model $\mathcal{L}_\mathrm{H}$, with lattice constant $a = 1$, dimensions $L \times L$, and periodic boundary conditions. Here, the simple translational symmetry and toroidal topology are expedient for numerical simulations. Next, we introduce a square removal lattice $\mathcal{L}_\rho$, with lattice constant $a_\rho = \sqrt{1/(1-\rho)}$, symmetrically offset from a chosen "origin" site of $\mathcal{L}_\mathrm{H}$, analogously to how $\mathcal{L}_\rho$ was offset on the disk in Eq. (2), as sketched in Fig. 5. For each site of the removal lattice $\mathbf{r}_{ij} \in \mathcal{L}_\rho$, we then find the corresponding most-localized state $|\psi_{ij}\rangle$ in the $\mathcal{L}_\mathrm{H}$ basis. In contrast to the continuous case, since $\mathcal{L}_\mathrm{H}$ and $\mathcal{L}_\rho$ are incommensurate lattices, we can no longer exploit conventional translation operators to simplify the computations. Instead, we compute the most-localized state at each $\mathbf{r}_{ij} \in \mathcal{L}_\rho$ by extracting the minimum-eigenvalue state of the distance-squared matrix $D_{ij}^2 = P_\mathrm{LB}(\mathbf{r} - \mathbf{r}_{ij})^2 P_\mathrm{LB}$, where P_LB is the projector to the lowest band. Furthermore, care needs to be taken when $\mathbf{r}_{ij}$ falls on an axis of $\mathcal{L}_\mathrm{H}$, since this can result in a two- or fourfold degeneracy for the minimum localization length. In these cases, we break the degeneracy to avoid any linear dependencies by selecting the state that has the smallest overlap with the previously selected states $\{|\psi\rangle\}$. Finally, due to the incommensurability of $\mathcal{L}_\mathrm{H}$ and $\mathcal{L}_\rho$, coupled with the periodic boundary conditions, we need to ensure that $\mathcal{L}_\rho$ does not have any overlapping regions.

Now that we have defined the set of maximally localized states in our Chern insulator for each removal iteration ρ, we can proceed to remove these states from the system. As before, we note that, although the most-localized states corresponding to our removal lattice $\mathcal{L}_\rho$ are generally linearly independent, they are not mutually orthogonal. Hence we first symmetrically orthogonalize the set of maximally localized states $\{|\psi\rangle\} \to \{|\tilde{\psi}\rangle\}$ and then project them out of the system, using

$$P_\rho^\mathrm{CI} = P_\mathrm{LB} - \sum_{i,j \in \mathcal{L}_\rho} |\tilde{\psi}_{ij}\rangle\langle\tilde{\psi}_{ij}|. \tag{6}$$

Note that this has the same form as the projector in Eq. (3) [39]. Finally, we record the localization length, which we quantify as the minimum eigenvalue of the distance-squared operator, with respect to the origin $D^2 = P_\rho^\mathrm{CI}\mathbf{r}^2 P_\rho^\mathrm{CI}$. In this case, care needs to be taken to ensure that we are minimizing distances on the torus. As before, we have designed our system such that the reference "origin" site hosts the most-localized remaining state and is least susceptible to numerical artifacts. We start with a large lattice constant with $\rho \lesssim 1$ and then symmetrically shrink the lattice by taking the limit $\rho \to 0$. In this limit, the $\mathcal{L}_\mathrm{H}$ and $\mathcal{L}_\rho$ interpenetrating lattices have the same lattice constant, which corresponds to the removal of a complete basis of states and hence a divergence of the localization length for a topological phase, in general [40].

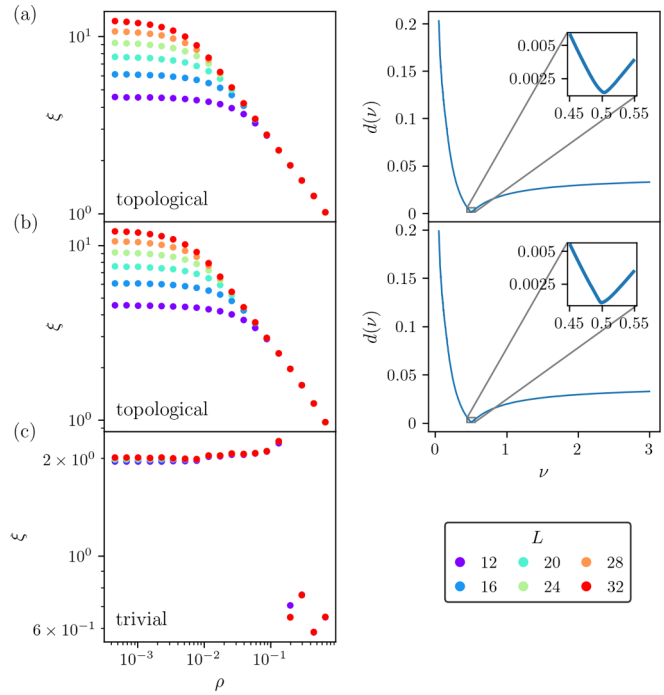

FIG. 6. Localization scaling in the Haldane model. (Left) Localization length $\xi(\rho)$ obtained by the simultaneous elimination of a lattice of localized degrees of freedom, applied to the Haldane model with parameters (a) $\mathbf{t}_a$, (b) $\mathbf{t}_b$, and (c) $\mathbf{t}_c$. The system size L is depicted in different colors. (Right) The quality function of data collapse $d(\nu)$ for systems in the topological Haldane model with parameters (a) $\mathbf{t}_a$ and (b) $\mathbf{t}_b$; optimization of the quality function results in critical exponents of (a) $\nu_{\mathbf{t}_a} = 0.503 \pm 0.011$ and (b) $\nu_{\mathbf{t}_b} = 0.499 \pm 0.012$.

3. Results

As before, we can plot the localization length ξ as a function of ρ under this iterative state removal. In Fig. 6, we present the localization scaling for our three parameter sets: $\mathbf{t}_a$, $\mathbf{t}_b$, and $\mathbf{t}_c$. Starting with the topological configurations shown in Figs. 6(a) and 6(b), we find a scaling relation similar to that observed for Landau levels in Fig. 2. That is, the localization length ξ exhibits a power-law divergence as the fraction of states remaining tends to zero $\rho \to 0$ in the thermodynamic limit $L \to \infty$, as shown in the left panels of Figs. 6(a) and 6(b). Furthermore, using a finite-size scaling ansatz, we can accurately compute the scaling exponent by minimizing a quality metric of data collapse, as shown in the right panels of Figs. 6(a) and 6(b). Here, we obtain scaling exponents of $\nu_{\mathbf{t}_a} = 0.503 \pm 0.011$ and $\nu_{\mathbf{t}_b} = 0.499 \pm 0.012$, where the error bars are given by 1% deviations with respect to the quality metric $d(\nu)$. As before, the scaling exponents take a value of $\nu \simeq 0.5$ in each case. Although the precision is

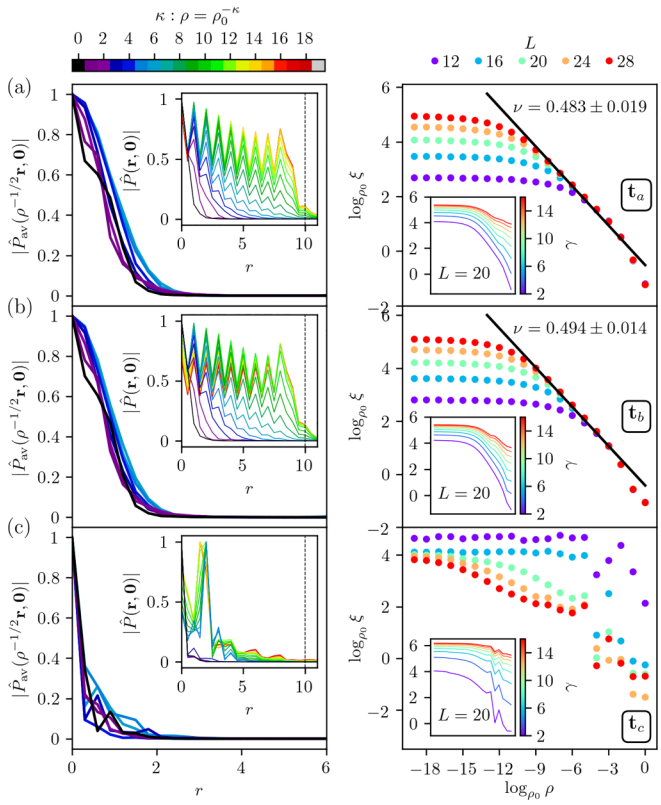

FIG. 7. Projector expansion in the Haldane model. (Left) Real-space radial profile of the projector $P(\mathbf{r},\mathbf{0}) = \langle \mathbf{r}|P_\rho^{\rm CI}|\mathbf{0}\rangle$. The rotationally and translationally averaged projector, normalized with respect to the initial value, $\hat{P}_{\rm av}$, is shown in the main plot. The original unaveraged projector, normalized with respect to the maximum value, $\hat{P}$, is shown inset. The projectors are presented for the (a) $\mathbf{t}_a$, (b) $\mathbf{t}_b$, and (c) $\mathbf{t}_c$ phases of the Haldane model, at a system size of $L = 28$ in the main plot and $L = 20$ in the inset, with $\rho_0 = 1.5$. The boundary of the system at $r = 10$ in the inset is marked with a dashed line. Note that the projectors are plotted in reverse order, such that the $\kappa = 0$ line is on top. (Right) Finite-size scaling of the second moment of the projector for the (a) $\mathbf{t}_a$, (b) $\mathbf{t}_b$, and (c) $\mathbf{t}_c$ phases of the Haldane model. The lines of best fit, for the linear region of the largest system size, are overlaid in black. The corresponding higher moments, $\xi^\gamma = \langle r^\gamma \rangle$, are shown inset for $L = 20$.

reduced due to the discrete nature of the systems, all computed values of ν from continuous and discrete topological systems agree within errors. In contrast, for the trivial configuration $\mathbf{t}_c$, shown in Fig. 6(c), we find that, as we decrease ρ, the localization length ξ quickly and abruptly converges to an L-independent constant [41]. This shows a sharp distinction to the behavior in topological phases, which supports the use of localization renormalization as an efficient numerical diagnostic for quantum Hall systems.

To gain further insight into the distinct scaling behavior in topological and trivial systems, we examine the expansion of the projector in real space. In the left panels of Fig. 7, we show the magnitude of the projector $|P(\mathbf{r},\mathbf{0})| = |\langle \mathbf{r}|P_\rho^{\rm CI}|\mathbf{0}\rangle|$ at each removal iteration ρ. Starting with the insets in the left panels of Figs. 7(a) and 7(b), we can see that in the topological phases of the Haldane model, the normalized projector $|\hat{P}| \sim \rho^{-1}|P|$ behaves analogously to the projector in the LLL, shown in the left inset of Fig. 3(ii)(a). We note that, in this case, the modulation of the normalized projector $\hat{P}$ due to $\mathcal{L}_0$, with length scale $a_0 = 1$, is exacerbated by the presence of the underlying lattice $\mathcal{L}_{\rm H}$. Starting with a Gaussian initial state at $\rho = 1$, we observe an expansion of the projector at each removal iteration, until the edge of the system ($r = 10$) is reached at $\rho \approx 1.5^{-9}$. This corresponds to where the power-law scaling of the $L = 20$ curves breaks down in the left panels of Figs. 6(a) and 6(b). As before, in the right panels of Figs. 7(a) and 7(b), we show that the second moment of the projector can be used as a proxy for the localization. From this data, we can extract the scaling exponents, which agree with those found in Fig. 6, albeit with larger errors due to the indirect nature of the computation. As for Landau levels, we find that this scaling holds not only for the second moment of the projector but also for higher moments, $\gamma \lesssim 10$, indicating statistical self-similarity, as shown in the right insets of Figs. 7(a) and 7(b). To elucidate this self-similarity, we plot the translationally and rotationally averaged normalized projector $\hat{P}_{\rm av}$, which eliminates any lattice artifacts, using rescaled coordinates $\mathbf{r}' = \rho^{-1/2}\mathbf{r}$ in the left panels of Figs. 7(a) and 7(b). Here, we observe that the family of projectors approximately collapse onto the initial Gaussian state. Although this collapse is not as clear as for the LLL case in the left panel of Fig. 3(ii)(a), due to the spatial discretization, the statistical agreement, in terms of moments, is comparable. In contrast, for the trivial phase of the Haldane model, shown in Fig. 7(c), we do not observe a self-similar expansion of the projector in the left inset. Instead, the projector quickly and abruptly converges to a fixed position as we decrease ρ. Attempting to extract the localization length via the second moment, as shown in the right panel, we obtain a convergence to an L-independent constant in agreement with Fig. 6(c). This demonstrates the difference between topological and trivial phases at the level of the projector. Just as localization length divergence in topological phases corresponds to self-similar projector expansion, the convergence of the localization length in trivial phases corresponds to projector convergence in real space.

IV. DISCUSSION

Following these results, in this section we discuss the scaling exponent. In particular, we comment on the RG framework of the truncation procedure in Sec. IV A, its analogy with the plateau transition in Sec. IV B, and its utility in diagnosing topological phases in Sec. IV C.

A. Real-space RG framework

As mentioned in Sec. II, in order for localization renormalization to hold, it is a necessary condition that we can construct a renormalized system $\{H', |\psi'\rangle\}$ from the original system $\{H, |\psi\rangle\}$. In the single-particle case, one way of demonstrating this is to show that the family of projectors P_ρ, defined in Eq. (1), is self-similar, which implies that the truncated system can be related to the original system under a coarse-graining, rescaling, and renormalization. By analyzing the expansion of real-space projectors on each ρ iteration, we have demonstrated that we can consolidate our state removal procedure into such an RG framework [42]. Each step of

removing the most-localized states in the system is analogous to coarse graining the Hamiltonian to an effective system of remaining states $\bar{H}(\mathbf{r}) = P_\rho H(\mathbf{r}) P_\rho$. Subsequently, we have shown, by studying the projectors in Figs. 3 and 7, that the system is statistically self-similar under a rescaling $\mathbf{r}' = \rho^{-1/2}\mathbf{r}$ and renormalization $H'(\mathbf{r}') = \rho^{-1}\bar{H}(\mathbf{r}')$. Although the projectors do not exhibit an exact self-similarity in our examples, they are statistically self-similar to a high degree—approximately up to the tenth moment in the configurations that we study. Moreover, since the localization length is conventionally defined via the second moment of displacement, it can be viewed as a self-similar property of the family of projectors P_ρ and localization renormalization may be applied.

B. Quantum Hall plateau transition

The most famous example of a localization transition induced by the topology-localization dichotomy in quantum Hall systems is the plateau transition and so it is natural to ask whether an analogy can be made with the localization scaling studied in this paper. Although these two concepts are fundamentally different, with the plateau transition yielding a universal scaling exponent of $\nu_{\mathrm{p}} \simeq 2.5$ [9,43–48], there are certain qualitative comparisons that can be drawn. In localization renormalization, we induce a phase transition by explicitly projecting out the most-localized states at individual points in space. On the other hand, in the plateau transition, we induce a phase transition by tuning the Fermi energy with respect to a disorder potential landscape. Loosely speaking, there is a correspondence between maximally localized states and states that are trapped around extrema in a disorder landscape. In this language, localization renormalization equates to trapping isolated states using equal-amplitude Dirac delta extrema in a fictitious potential, whereas the plateau transition equates to trapping eigenstates of a real disorder potential $V(\mathbf{r}) \approx \sum_i V_i \delta(\mathbf{r} - \mathbf{r}_i)$, where V_i is a random amplitude at position $\mathbf{r}_i$. Although localization renormalization is a numerical algorithm and does not correspond to a physically motivated phase transition, it would be interesting to explore this analogy in future work [18,19].

C. Topological phase diagnosis

The broad scope of the localization renormalization procedure is to classify a variety of condensed matter phases using universal scaling exponents. Based on our results, we conjecture that $\nu \sim 1/2$ for all two-dimensional class A topological insulators and we generally expect different scaling exponents in other symmetry classes and dimensions, e.g., $\nu \sim 1/d$. However, although the procedure is designed as a numerical tool to study a diverse selection of localization transitions, the examples shown in this paper are all centered on the topology-localization dichotomy and so the method doubles as a technique for diagnosing topological and trivial phases. This has a number of advantages compared to conventional approaches, such as computing edge modes or the Chern number. For example, the algorithm is spectrum independent and so may be used to diagnose topology in disordered systems, provided the disorder is sufficiently weak so as to not mix the bands. Moreover, the method is numerically inexpensive, with a clear power-law divergence and scaling exponent reported after only the first few removal iterations [49]. These advantages can prove particularly useful in cases where the phase diagram is unknown or traditional methods for computing the Chern number fail, such as in fractal lattices [50], hyperbolic lattices [51], and quasicrystals [52], as well as in systems with other symmetry classes or higher dimensions.

V. CONCLUSION

We have introduced the localization renormalization formalism as a way of analyzing a diverse range of localization transitions, which we demonstrated numerically using integer quantum Hall examples. By iteratively removing an orthogonal subset of maximally localized states from distinct sites, we can induce quantum Hall breakdown transitions with a localization length divergence of $\lim_{\rho\to 0, L\to\infty} \xi(\rho) \sim \rho^{-\nu}$ with $\nu = 0.5$ in topological systems and convergence to a system-size-independent constant in the trivial case. The scaling exponent in these topological systems is universal and therefore independent of the model used to describe the system, the metric used to define the localization length, and the details of the state removal algorithm. Moreover, by analyzing the expansion of real-space projectors on each iteration, we find that the scaling exponent is a self-similar property of the family of projectors P_ρ, which is in accord with an RG picture. This motivates the use of localization renormalization as a versatile diagnostic tool for quantum Hall systems, in cases where traditional methods of diagnosing band topology are inadequate, as well as in topologically trivial systems and beyond.

ACKNOWLEDGMENTS

We thank G. Wagner, S. Garratt, M. Zaletel, A. Culver, P. Sathe, D. Bauer, A. Brown, X. Liu, and S. Talkington for useful discussions. In particular, we thank G. Wagner and S. Garratt for helpful comments on the manuscript. Preliminary results from this work are presented in the Ph.D. thesis of D.R. [53]. B.A. acknowledges support from the Swiss National Science Foundation under Grant No. P500PT_203168; B.A. and R.R. acknowledge support from the University of California Laboratory Fees Research Program funded by the UC Office of the President (UCOP), Grant ID No. LFR-20-653926; D.R., F.H., and R.R. acknowledge support from the NSF under CAREER Grant No. DMR-1455368 and the Alfred P. Sloan foundation; all authors thank the Mani L. Bhaumik Institute for Theoretical Physics.

[1] B. Swingle and J. McGreevy, Renormalization group constructions of topological quantum liquids and beyond, Phys. Rev. B **93**, 045127 (2016).

[2] S. R. White, Density matrix formulation for quantum renormalization groups, Phys. Rev. Lett. **69**, 2863 (1992).

[3] C. Wetterich, Exact evolution equation for the effective potential, Phys. Lett. B **301**, 90 (1993).

[4] G. Vidal, Class of quantum many-body states that can be efficiently simulated, Phys. Rev. Lett. **101**, 110501 (2008).

[5] M. Koch-Janusz and Z. Ringel, Mutual information, neural networks and the renormalization group, Nat. Phys. **14**, 578 (2018).

[6] L. Guo, Y. Chen, S. Shi, and B. J. West, Renormalization group and fractional calculus methods in a complex world: A review, Fract. Calc. Appl. Anal. **24**, 5 (2021).

[7] B. Sbierski, E. J. Dresselhaus, J. E. Moore, and I. A. Gruzberg, Criticality of two-dimensional disordered Dirac fermions in the unitary class and universality of the integer quantum Hall transition, Phys. Rev. Lett. **126**, 076801 (2021).

[8] K. S. Huang, S. Raghu, and P. Kumar, Numerical study of a dual representation of the integer quantum Hall transition, Phys. Rev. Lett. **126**, 056802 (2021).

[9] Q. Zhu, P. Wu, R. N. Bhatt, and X. Wan, Localization-length exponent in two models of quantum Hall plateau transitions, Phys. Rev. B **99**, 024205 (2019).

[10] M. R. Zirnbauer, The integer quantum Hall plateau transition is a current algebra after all, Nucl. Phys. B **941**, 458 (2019).

[11] I. García-Mata, J. Martin, O. Giraud, B. Georgeot, R. Dubertrand, and G. Lemarié, Critical properties of the Anderson transition on random graphs: Two-parameter scaling theory, Kosterlitz-Thouless type flow, and many-body localization, Phys. Rev. B **106**, 214202 (2022).

[12] T. Thiery, F. Huveneers, M. Müller, and W. De Roeck, Many-body delocalization as a quantum avalanche, Phys. Rev. Lett. **121**, 140601 (2018).

[13] X. Guo and X. Li, Detecting many-body-localization lengths with cold atoms, Phys. Rev. A **97**, 033622 (2018).

[14] R. Modak, S. Ghosh, and S. Mukerjee, Criterion for the occurrence of many-body localization in the presence of a single-particle mobility edge, Phys. Rev. B **97**, 104204 (2018).

[15] S. Pu, G. J. Sreejith, and J. K. Jain, Anderson localization in the fractional quantum Hall effect, Phys. Rev. Lett. **128**, 116801 (2022).

[16] M.-Y. Li and P. Ye, Hierarchy of entanglement renormalization and long-range entangled states, Phys. Rev. B **107**, 115169 (2023).

[17] D. Bauer, S. Talkington, F. Harper, B. Andrews, and R. Roy, Fractional Chern insulators with a non-Landau level continuum limit, Phys. Rev. B **105**, 045144 (2022).

[18] H. Liu, C. Fulga, E. J. Bergholtz, and J. Asboth, Topological fine structure of an energy band, arXiv:2312.08436.

[19] J. Mildner, M. D. Caio, G. Möller, N. R. Cooper, and M. J. Bhaseen, Topological phase transitions in the disordered Haldane model, arXiv:2312.16689.

[20] N. Marzari and D. Vanderbilt, Maximally localized generalized Wannier functions for composite energy bands, Phys. Rev. B **56**, 12847 (1997).

[21] E. I. Rashba, L. E. Zhukov, and A. L. Efros, Orthogonal localized wave functions of an electron in a magnetic field, Phys. Rev. B **55**, 5306 (1997).

[22] Note that the size of the removal subregion corresponding to a complete set of states, $|\mathcal{L}_0|$, is not necessarily equal to the size of the region $|A|$, as shown for Landau levels in Sec. III A 1.

[23] See Supplemental Material at http://link.aps.org/supplemental/10.1103/PhysRevB.109.125132 for details of the symmetric orthogonalization procedure, alternative methods to truncate the single-particle basis, alternative removal lattices for the truncation algorithm, alternative methods to compute the localization length, the theory of finite-size scaling, the statistical moments method for computing the localization length, and the parameter dependence of localization scaling in Chern insulators. The Supplemental Material also contains Refs. [32,33,54–62].

[24] Similarly, in the case of multicomponent systems, we can choose a composite wave function basis $\{|\psi^c\rangle\}$ to define the procedure.

[25] D. Yoshioka, *The Quantum Hall Effect* (Springer, Berlin, 1998).

[26] B. Andrews, Stability of topological states and crystalline solids, Ph.D. thesis, University of Cambridge, 2019.

[27] I. A. Malkin and V. I. Man'ko, Coherent states of a charged particle in a magnetic field, JETP **28**, 527 (1969).

[28] A. M. Perelomov, On the completeness of a system of coherent states, Theor. Math. Phys. **6**, 156 (1971).

[29] From now on, we work in natural units.

[30] In the original paper by Perelomov [28], they work in the space of complex eigenvalues β to obtain a critical unit cell area $S = \pi$. However, in real space, the wave packets are centered at coordinates $\mathbf{r}_\beta = \sqrt{2}[\mathrm{Re}(\beta), \mathrm{Im}(\beta)]$, which yields a critical unit cell area $S = 2\pi$.

[31] Note that the order of limits is not significant.

[32] S. M. Bhattacharjee and F. Seno, A measure of data collapse for scaling, J. Phys. A **34**, 6375 (2001).

[33] J. A. Nelder and R. Mead, A simplex method for function minimization, Comput. J. **7**, 308 (1965).

[34] We note that a local maximum emerges as we increase $\gamma \gtrsim 10$, which breaks the linear scaling at large ρ. Although it is difficult to interpret higher-order moments visually, this effect may be due to the critical lattice modulation causing a proportionally larger distortion of projectors with smaller radii.

[35] Self-similarity is mathematically defined for all moments, so that distributions are statistically identical. However, in practice, the definition is often taken to refer to the first two moments only [63–66].

[36] F. D. M. Haldane, Model for a quantum Hall effect without Landau levels: Condensed-matter realization of the "parity anomaly", Phys. Rev. Lett. **61**, 2015 (1988).

[37] S. H. Simon and M. S. Rudner, Contrasting lattice geometry dependent versus independent quantities: Ramifications for Berry curvature, energy gaps, and dynamics, Phys. Rev. B **102**, 165148 (2020).

[38] W. Zhao, K. Kang, L. Li, C. Tschirhart, E. Redekop, K. Watanabe, T. Taniguchi, A. Young, J. Shan, and K. F. Mak, Realization of the Haldane Chern insulator in a moiré lattice, Nat. Phys. **20**, 275 (2024).

[39] Although the dimension of P_ρ^{CI} is $2L^2$, its rank is at most L^2 due to the band projection.

[40] T. M. Gunawardana, A. M. Turner, and R. Barnett, Optimally localized Wannier functions for 2D Chern insulators, arXiv:2309.07242.

[41] The localization length converges to a system-size-independent constant following a nonuniversal readjustment regime, which is sensitive to numerical parameters.

[42] L. P. Kadanoff, Scaling laws for Ising models near T_c, Phys. Phys. Fiz. **2**, 263 (1966).

[43] H. P. Wei, D. C. Tsui, M. A. Paalanen, and A. M. M. Pruisken, Experiments on delocalization and university in the integral quantum Hall effect, Phys. Rev. Lett. **61**, 1294 (1988).
[44] W. Li, C. L. Vicente, J. S. Xia, W. Pan, D. C. Tsui, L. N. Pfeiffer, and K. W. West, Scaling in plateau-to-plateau transition: A direct connection of quantum Hall systems with the Anderson localization model, Phys. Rev. Lett. **102**, 216801 (2009).
[45] J. T. Chalker and P. D. Coddington, Percolation, quantum tunnelling and the integer Hall effect, J. Phys. C **21**, 2665 (1988).
[46] B. Huckestein, B. Kramer, and L. Schweitzer, Characterization of the electronic states near the centres of the Landau bands under quantum Hall conditions, Surf. Sci. **263**, 125 (1992).
[47] Y. Huo and R. N. Bhatt, Current carrying states in the lowest Landau level, Phys. Rev. Lett. **68**, 1375 (1992).
[48] K. Slevin and T. Ohtsuki, Critical exponent for the quantum Hall transition, Phys. Rev. B **80**, 041304(R) (2009).
[49] Provided that the parameter set is sufficiently far from a phase transition.
[50] M. C. Jha and A. E. B. Nielsen, Properties of Laughlin states on fractal lattices, J. Stat. Mech.: Theory Exp. (2023) 053103.
[51] W. Zhang, F. Di, X. Zheng, H. Sun, and X. Zhang, Hyperbolic band topology with non-trivial second Chern numbers, Nat. Commun. **14**, 1083 (2023).
[52] M. Koshino and H. Oka, Topological invariants in two-dimensional quasicrystals, Phys. Rev. Res. **4**, 013028 (2022).
[53] D. Reiss, Analytical and numerical techniques in static and driven topological matter, Ph.D. thesis, UCLA, 2020.
[54] P.-O. Löwdin, On the nonorthogonality problem, *Advances in Quantum Chemistry* (Elsevier, Amsterdam, 1970), Vol. 5, pp. 185–199.
[55] B. C. Carlson and J. M. Keller, Orthogonalization procedures and the localization of Wannier functions, Phys. Rev. **105**, 102 (1957).
[56] I. Mayer, On Löwdin's method of symmetric orthogonalization, Int. J. Quantum Chem. **90**, 63 (2002).
[57] M. E. Fisher and M. N. Barber, Scaling theory for finite-size effects in the critical region, Phys. Rev. Lett. **28**, 1516 (1972).
[58] V. Privman, *Finite Size Scaling and Numerical Simulation of Statistical Systems* (World Scientific, Singapore, 1990).
[59] M. E. J. Newman and G. T. Barkema, *Monte Carlo Methods in Statistical Physics* (Clarendon Press, Oxford, 1999).
[60] N. Kawashima and N. Ito, Critical behavior of the three-dimensional J model in a magnetic field, J. Phys. Soc. Jpn. **62**, 435 (1993).
[61] J. Houdayer and A. K. Hartmann, Low-temperature behavior of two-dimensional Gaussian Ising spin glasses, Phys. Rev. B **70**, 014418 (2004).
[62] S. Wenzel, E. Bittner, W. Janke, and A. M. Schakel, Percolation of vortices in the 3D Abelian lattice Higgs model, Nucl. Phys. B **793**, 344 (2008).
[63] P. Embrechts and M. Maejima, An introduction to the theory of self-similar stochastic processes, Int. J. Mod. Phys. B **14**, 1399 (2000).
[64] C.-k. Peng, J. M. Hausdorff, and A. L. Goldberger, Fractal mechanisms in neuronal control: human heartbeat and gait dynamics in health and disease, in *Self-Organized Biological Dynamics and Nonlinear Control: Toward Understanding Complexity, Chaos and Emergent Function in Living Systems*, edited by J. Walleczek (Cambridge University Press, Cambridge, UK, 2000), pp. 66–96.
[65] B. Mandelbrot and R. Hudson, *The (Mis)Behaviour of Markets: A Fractal View of Risk, Ruin and Reward* (Profile, London, 2010).
[66] B. Andrews and G. Möller, Self-similarity of spectral response functions for fractional quantum Hall states, Proc. R. Soc. A **479**, 20230021 (2023).